

Special Issue: Polymers for Microelectronics

Guest Editors: Dr Brian Knapp (Promerus LLC) and
Prof. Paul A. Kohl (Georgia Institute of Technology)

EDITORIAL

Polymers for Microelectronics

B. Knapp and P. A. Kohl, *J. Appl. Polym. Sci.* 2014, DOI: [10.1002/app.41233](https://doi.org/10.1002/app.41233)

REVIEW

Negative differential conductance materials for flexible electronics

A. Nogaret, *J. Appl. Polym. Sci.* 2014, DOI: [10.1002/app.40169](https://doi.org/10.1002/app.40169)

RESEARCH ARTICLES

Generic roll-to-roll compatible method for insolubilizing and stabilizing conjugated active layers based on low energy electron irradiation

M. Helgesen, J. E. Carlé, J. Helt-Hansen, A. Miller, and F. C. Krebs, *J. Appl. Polym. Sci.* 2014, DOI: [10.1002/app.40795](https://doi.org/10.1002/app.40795)

Selective etching of polylactic acid in poly(styrene)-block-poly(D,L)lactide diblock copolymer for nanoscale patterning

C. Cummins, P. Mokarian-Tabari, J. D. Holmes, and M. A. Morris, *J. Appl. Polym. Sci.* 2014, DOI: [10.1002/app.40798](https://doi.org/10.1002/app.40798)

Preparation and dielectric behavior of polyvinylidene fluoride composite filled with modified graphite nanoplatelet

P. Xie, Y. Li, and J. Qiu, *J. Appl. Polym. Sci.* 2014, DOI: [10.1002/app.40229](https://doi.org/10.1002/app.40229)

Design of a nanostructured electromagnetic polyaniline–Keggin iron–clay composite modified electrochemical sensor for the nanomolar detection of ascorbic acid

R. V. Lilly, S. J. Devaki, R. K. Narayanan, and N. K. Sadanandhan, *J. Appl. Polym. Sci.* 2014, DOI: [10.1002/app.40936](https://doi.org/10.1002/app.40936)

Synthesis and characterization of novel phosphorous-silicone-nitrogen flame retardant and evaluation of its flame retardancy for epoxy thermosets

Z.-S. Li, J.-G. Liu, T. Song, D.-X. Shen, and S.-Y. Yang, *J. Appl. Polym. Sci.* 2014, DOI: [10.1002/app.40412](https://doi.org/10.1002/app.40412)

Electrical percolation behavior and electromagnetic shielding effectiveness of polyimide nanocomposites filled with carbon nanofibers

L. Nayak, T. K. Chaki, and D. Khastgir, *J. Appl. Polym. Sci.* 2014, DOI: [10.1002/app.40914](https://doi.org/10.1002/app.40914)

Morphological influence of carbon modifiers on the electromagnetic shielding of their linear low density polyethylene composites

B. S. Villacorta and A. A. Ogale, *J. Appl. Polym. Sci.* 2014, DOI: [10.1002/app.41055](https://doi.org/10.1002/app.41055)

Electrical and EMI shielding characterization of multiwalled carbon nanotube/polystyrene composites

V. K. Sachdev, S. Bhattacharya, K. Patel, S. K. Sharma, N. C. Mehra, and R. P. Tandon, *J. Appl. Polym. Sci.* 2014, DOI: [10.1002/app.40201](https://doi.org/10.1002/app.40201)

Anomalous water absorption by microelectronic encapsulants due to hygrothermal-induced degradation

M. van Soestbergen and A. Mavinkurve, *J. Appl. Polym. Sci.* 2014, DOI: [10.1002/app.41192](https://doi.org/10.1002/app.41192)

Design of cyanate ester/azomethine/ZrO₂ nanocomposites high-k dielectric materials by single step sol-gel approach

M. Ariraman, R. Sasi Kumar and M. Alagar, *J. Appl. Polym. Sci.* 2014, DOI: [10.1002/app.41097](https://doi.org/10.1002/app.41097)

Furan/imide Diels–Alder polymers as dielectric materials

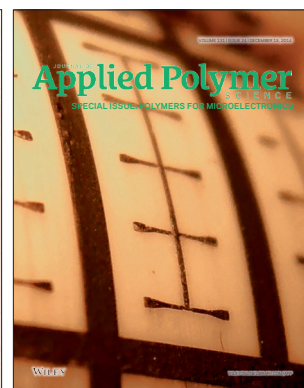
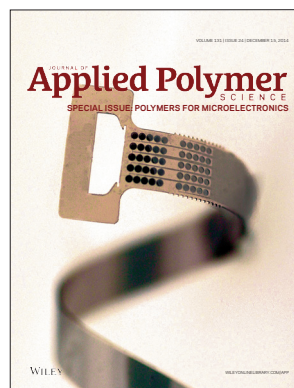
R. G. Lorenzini and G. A. Sotzing, *J. Appl. Polym. Sci.* 2014, DOI: [10.1002/app.40179](https://doi.org/10.1002/app.40179)

High dielectric constant polyimide derived from 5,5'-bis[(4-amino) phenoxy]-2,2'-bipyrimidine

X. Peng, Q. Wu, S. Jiang, M. Hanif, S. Chen, and H. Hou, *J. Appl. Polym. Sci.* 2014, DOI: [10.1002/app.40828](https://doi.org/10.1002/app.40828)

The influence of rigid and flexible monomers on the physical-chemical properties of polyimides

T. F. da Conceição and M. I. Felisberti, *J. Appl. Polym. Sci.* 2014, DOI: [10.1002/app.40351](https://doi.org/10.1002/app.40351)



Special Issue: Polymers for Microelectronics

Guest Editors: Dr Brian Knapp (Promerus LLC) and
Prof. Paul A. Kohl (Georgia Institute of Technology)

Development of polynorbornene as a structural material for microfluidics and flexible BioMEMS

A. E. Hess-Dunning, R. L. Smith, and C. A. Zorman, *J. Appl. Polym. Sci.* 2014, DOI: [10.1002/app.40969](https://doi.org/10.1002/app.40969)

A thin film encapsulation layer fabricated via initiated chemical vapor deposition and atomic layer deposition

B. J. Kim, D. H. Kim, S. Y. Kang, S. D. Ahn, and S. G. Im, *J. Appl. Polym. Sci.* 2014, DOI: [10.1002/app.40974](https://doi.org/10.1002/app.40974)

Surface relief gratings induced by pulsed laser irradiation in low glass-transition temperature azopolysiloxanes

V. Damian, E. Resmerita, I. Stoica, C. Ibanescu, L. Sacarescu, L. Rocha, and N. Hurduc, *J. Appl. Polym. Sci.* 2014, DOI: [10.1002/app.41015](https://doi.org/10.1002/app.41015)

Polymer-based route to ferroelectric lead strontium titanate thin films

M. Benkler, J. Hobmaier, U. Gleißner, A. Medesi, D. Hertkorn, and T. Hanemann, *J. Appl. Polym. Sci.* 2014, DOI: [10.1002/app.40901](https://doi.org/10.1002/app.40901)

The influence of dispersants that contain polyethylene oxide groups on the electrical resistivity of silver paste

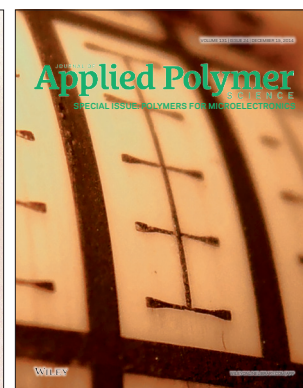
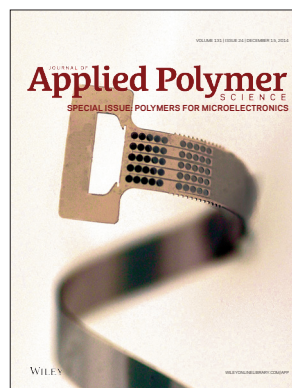
T. H. Chiang, Y.-F. Chen, Y. C. Lin, and E. Y. Chen, *J. Appl. Polym. Sci.* 2014, DOI: [10.1002/app.41183](https://doi.org/10.1002/app.41183)

Quantitative investigation of the adhesion strength between an SU-8 photoresist and a metal substrate by scratch tests

X. Zhang, L. Du, and M. Zhao, *J. Appl. Polym. Sci.* 2014, DOI: [10.1002/app.41108](https://doi.org/10.1002/app.41108)

Thermodynamic and kinetic aspects of defectivity in directed self-assembly of cylinder-forming diblock copolymers in laterally confining thin channels

B. Kim, N. Laachi, K. T. Delaney, M. Carilli, E. J. Kramer, and G. H. Fredrickson, *J. Appl. Polym. Sci.* 2014, DOI: [10.1002/app.40790](https://doi.org/10.1002/app.40790)



Thermodynamic and Kinetic Aspects of Defectivity in Directed Self-Assembly of Cylinder-Forming Diblock Copolymers in Laterally Confining Thin Channels

Bongkeun Kim,¹ Nabil Laachi,¹ Kris T. Delaney,¹ Michael Carilli,² Edward J. Kramer,^{1,3} Glenn H. Fredrickson^{1,3}

¹Materials Research Laboratory, University of California, Santa Barbara, California 93106

²Department of Physics, University of California, Santa Barbara, California 93106

³Departments of Chemical Engineering and Materials, University of California, Santa Barbara, California 93106

Correspondence to: G. H. Fredrickson (E-mail: ghf@mrl.ucsb.edu)

ABSTRACT: We use self-consistent field theory to calculate the energy of defect formation in cylinder-forming diblock copolymers in laterally confining thin channels. We focus on two isolated defects, dislocations and disclinations and explore a wide range of polymer and channel characteristics. Our findings suggest appropriate conditions for the design of optimized graphoepitaxial processes, where defects are limited to very low concentrations. Using the string method, we also investigate the energy barriers and kinetic pathways of the transition from defective to perfect states. © 2014 Wiley Periodicals, Inc. *J. Appl. Polym. Sci.* **2014**, *131*, 40790.

KEYWORDS: copolymers; films; nanostructured polymers; polystyrene; self-assembly

Received 27 February 2014; accepted 1 April 2014

DOI: 10.1002/app.40790

INTRODUCTION

The self-assembly of block copolymers (BCPs) has emerged in recent years as a promising patterning tool to overcome the scaling limits in nanolithography and generate suboptical lithographic patterns.^{1–10} In the absence of controlled external guidance, block copolymer thin films with lamellar or cylindrical morphologies exhibit poor long-range order because of thermally excited long wavelength phonon modes that disrupt the ordering process.^{1,11–13} Directed self-assembly (DSA) using chemical or topological features on the film substrate has consequently become an important focus of the advanced lithography community, with the objective of reducing defect densities below the requirements of the semiconductor industry (<0.01 defects/cm²).¹⁴

While electric fields,¹⁵ flow,¹⁶ and shear application¹⁷ have all been successfully used to direct alignment in microdomain structures, chemically prepatterned surfaces (*chemoepitaxy*)^{18,19} and topographical confinement (*graphoepitaxy*)¹² are two potentially inexpensive and industry-compatible techniques that can dramatically reduce the defect density in both lamella- and cylinder-forming block copolymer thin films. While these epitaxial techniques can achieve long-range alignment of microdomains in BCP self-assembly,^{5,20,21} defects are not completely eliminated in the resulting patterns.

The directed self-assembly (DSA) of diblock copolymers into line and space patterns has been demonstrated both experimentally²² and theoretically^{23,24} with several preferential wetting conditions.^{22,25} Park et al.¹¹ produced well-ordered lamellar structure of polystyrene-*b*-methymethacrylate (PS-*b*-PMMA) block copolymers with up to eight periods in confining channels and found defective structures in the middle of wide channels. Ruiz et al.²⁵ reported ten periods of perfect lamellae in channels using a smaller molecular weight of PS-*b*-PMMA. The formation energy of isolated defects in lamella-forming diblock copolymers has also been estimated theoretically²⁶ and experimentally.²⁷ For example, lamellar structures were obtained on striped substrates with an estimated defect formation energy of 0.02 kT per nm².^{19,28} Using SCFT calculations, Takahashi et al.²⁹ reported defect formation energies ranging from ≈50 to ≈90 kT for isolated dislocation pairs and ≈100 to ≈120 kT for isolated disclinations in lamellar PS-*b*-PMMA block copolymers under lateral confinement. Using the string method,^{30,31} they also found kinetic barriers less than 10 kT for the transition from defective to perfect states. In cylinder-forming block copolymers, Hammond and co-workers²⁷ reported experimental estimates of defect formation energies of ≈14 kT in polystyrene-*b*-2-polyvinylpyridine (PS-*b*-P2VP) systems and Mishra and co-workers³² extended the range from ≈10 to ≈14 kT when varying the volume fraction of the blocks and the Flory–Huggins interaction parameter.

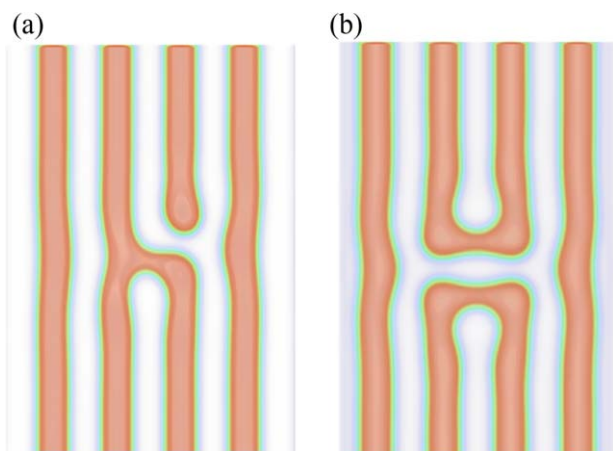


Figure 1. Examples of profiles of the PMMA block (in orange) under lateral confinement, showing a “dislocation” in (a) and a “disclination” in (b). [Color figure can be viewed in the online issue, which is available at wileyonlinelibrary.com.]

In this study, we focus on cylinder-forming AB diblock copolymers with a degree of polymerization N and a minor-block fraction f_A , laterally confined in narrow trenches with tunable, but homogeneous wetting conditions at the sidewalls and the top and bottom surfaces of the channel. Such selective affinities can be obtained experimentally using the “lift-off” technique¹¹ or by use of a bilayer substrate,³³ for example. The model equations governing the self-assembly a melt of AB diblock copolymers in confinement are based on the standard Gaussian-chain model, with a Flory-type monomer–monomer interaction parameter, χ , describing interactions between dissimilar (A and B) segments and Flory-like monomer–wall interaction parameters, χ_{wK} , describing interactions between K -type segments and the confining walls ($K = A$ or B). A particle-based model for a system of interacting polymer chains is converted into a field-based model of a single chain in an external field through a formally exact Hubbard–Stratonovich transformation. The resulting statistical field theory is simplified by imposing a mean-field approximation, resulting in the well-known equations of self-consistent-field theory (SCFT).³⁴ Details of the SCFT equations for a confined melt and the computational implementation can be found in the literature.^{23,35} Using our SCFT simulations, a large number of defects can be generated from random seeds but we focus in this study on two specific isolated defects, “dislocations” and “disclinations” because they are abundantly observed experimentally and can be more easily stabilized over a wide range of channel and polymer parameters. The density profiles of the two defects shown in Figure 1 indicate that the “dislocation” is in fact a tight dislocation pair and the “disclination” is composed of two disclinations bound to a large Burger vector dislocation.

We should mention at this point that our SCFT simulations produce a free energy per chain for a given set of parameters and morphology. One therefore needs to estimate the number of chains inside the simulation volume to compute the *extensive* free energy of the morphology, which is required to compute defect formation energies. For an incompressible AB melt in a volume V , the number of chains is given by:

$$n = \frac{V}{N(f_A m_A / \rho_A + f_B m_B / \rho_B)} \quad (1)$$

where m_K and ρ_K are the mass and the mass density of segments of type K ($K = A, B$). Since PS-*b*-PMMA is the most widely used polymer in DSA and for consistency with our previous results,²⁹ we use PS-*b*-PMMA as the reference polymer “1” for free energy calculations. For a given segregation strength χN and A-fraction f_A , the extensive free energy of a morphology in a different block copolymer system “2” (with a different χ value) can be obtained from that of system “1” at the same χN and f_A values using the conversion factor:

$$\frac{F_2}{F_1} = \frac{n_2}{n_1} = \frac{V_2 N_1}{V_1 N_2} \quad (2a)$$

where we have adopted a common average monomer volume, $v_0 = f_A m_A / \rho_A + f_B m_B / \rho_B$, for the two systems. Furthermore, because the results are presented for our reference system using film dimensions expressed in units of the chain radius of gyration R_g , the two systems should be compared at the same reduced film volumes $\tilde{V}_i = V_i / R_g^3$. Hence, the conversion factor becomes

$$\frac{F_2}{F_1} = \frac{V_2 N_1}{V_1 N_2} = \frac{N_1 R_{g2}^3}{N_2 R_{g1}^3} \approx \left(\frac{N_2}{N_1} \right)^{1/2} = \left(\frac{\chi_1}{\chi_2} \right)^{1/2} \quad (2b)$$

where in the fourth expression we have neglected differences in statistical segment lengths between the two systems.³⁴ As an example of the application of this formula, in order to compare with available experimental results for PS-*b*-P2VP cylinder-forming confined melts, the defect energies presented here must be rescaled using a multiplying factor of 0.58, which accounts for the differences in χ parameters between PS-*b*-P2VP and PS-*b*-PMMA. In the case of polystyrene-*b*-polydimethylsiloxane (PS-*b*-PDMS) block copolymers, the conversion factor is 0.35.

The main goal of our study is to determine, from a wide range of parameters of segregation strengths, polymer compositions, channel dimensions, and wetting configurations, the most suitable set that favors the formation of a monolayer of defect-free, horizontal (lying down) cylinders, both thermodynamically and kinetically. The remainder of the manuscript is organized as follows. In the next section, we consider confining trenches with A-attractive sidewalls and neutral top and bottom surfaces. This configuration allows a direct comparison with lamella-forming systems for both commensurability aspects and defectivity calculations.²⁹ In section “DSA in A-Attractive Sidewalls and Bottom Substrates and B-Attractive Top Surfaces”, selectivity is introduced at the top and bottom surfaces and our results will be compared to experimental results of Mishra et al.³² with PS-*b*-PV2P polymers under similar wetting conditions. In section “Optimal Wetting Conditions DSA in Narrow Trenches”, we present an extensive exploration of wetting configurations and determine the best conditions for cylinder formation with minimal defectivity. Beyond thermodynamic aspects, we also introduce in section “Defect Kinetics: Transition Pathways and Kinetic Barriers” calculations based on the string method to determine kinetic pathways for the melting of the defects into perfect structures.

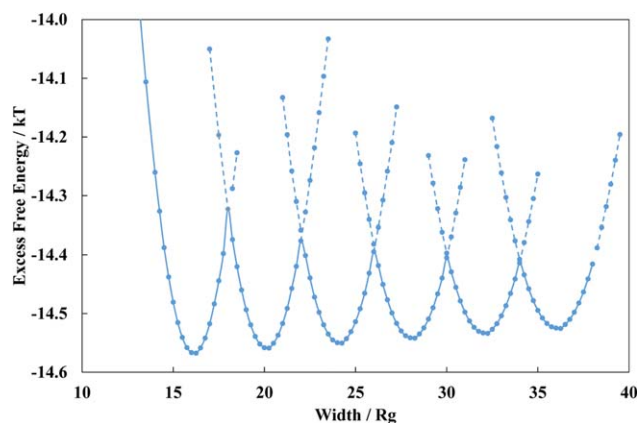


Figure 2. Plots of the excess free energy of perfectly aligned cylinders due to confinement in narrow trenches of height $3.75 R_g$ and various widths. Windows of commensurability are shown for 3–8 cylindrical periods. Here, $\chi N = 25$, $f_A = 0.3$, the sidewalls are A-attractive ($\chi_{wA} = -32$) and the top and bottom are neutral. [Color figure can be viewed in the online issue, which is available at wileyonlinelibrary.com.]

DSA IN A-ATTRACTIVE SIDEWALLS AND NEUTRAL TOP AND BOTTOM SURFACES

We first consider a confining channel with A-block-attractive sidewalls and neutral top and bottom surfaces. This wetting configuration is usually most suitable for the formation of standing-up lamellae in lamella-forming block copolymers^{27,29,36} and thus enables a direct comparison with results of commensurability and defectivity from our previous study on lamella-forming PS-b-PMMA in similar narrow trenches.²⁸

Commensurability

Before we discuss defectivity of cylinder-forming block copolymers in narrow trenches, we determine in this section commensurability windows for the perfect alignment of horizontal cylinders. Similar to commensurability calculations in lamella-forming systems,²⁸ optimal windows are determined by computing the excess free energy of the perfect cylinder arrangement in the trench relative to unconfined, bulk configurations. In the present case, the A-attractive sidewalls induce cylinder formation very easily from a random initial seed so it is straightforward to achieve perfectly aligned cylinders for various polymer compositions and channel dimensions. The minima of the excess free energies, which include surface and bulk film contributions, thus correspond to optimal channel widths and heights that favor monolayer films of horizontal cylinders. In the case of PS-b-PMMA block copolymers with a segregation strength, $\chi N = 25$, and a PMMA-block fraction, $f_A = 0.25$, confined in trenches with PMMA-attractive sidewalls ($\chi_{wA} N = -32$ and $\chi_{wB} N = 0$) and neutral top and bottom surfaces, commensurability calculations lead to an optimal channel height = $3.75 R_g$, where R_g denotes the radius of gyration of the polymer, which, under the present conditions, is ≈ 8 nm. This is slightly smaller than the bulk domain spacing, $w_0 = 4 R_g$, for a block copolymer with similar values of χN and f_A .

For the optimized channel height, we plot in Figure 2 the excess free energy as a function of the channel width when 3–8

cylindrical periods are stabilized inside the trench. As can be seen in Figure 2 the formation of a given number of cylindrical periods is limited to a well-defined window of commensurability. Inside each domain of width approximately $4 R_g$, the excess free energy has a minimum at the center of the window whereby the elastic component of the excess free energy is zero while the residual free energy is due to surface tension. Away from the optimal width, with the application of either compressive or tensile strains, elastic stresses build up in the polymer and ultimately lead to the creation or removal of a cylindrical period.

Note that similar width commensurability aspects arise in lamella-forming block copolymers in comparable trenches.²⁹ In contrast, the height of the channel does not affect the formation of lamellae, provided the top and bottom surfaces remain neutral.

Defectivity

We examine in this section the effect of polymer composition and channel width on the defect formation energy in cylinder-forming systems and compare our findings with previously reported calculations in lamella-forming block copolymers.²⁹ We therefore consider a PS-b-PMMA block copolymer with $\chi N = 25$ and various PMMA fractions, $f_A = 0.23, 0.24$, and 0.25 . The trench width is varied within a 4-period commensurability window while the height and the wetting conditions are the same as those used in the above commensurability calculations. Using our 3D SCFT simulations, dislocation defects could only be stabilized for $f_A = 0.25$ and all defective seeds for $f_A = 0.23$ and 0.24 resulted in perfect morphologies, preventing calculations of defect formation energies. Disclinations were however successfully stabilized for all fractions. The resulting formation energies are plotted in Figure 3.

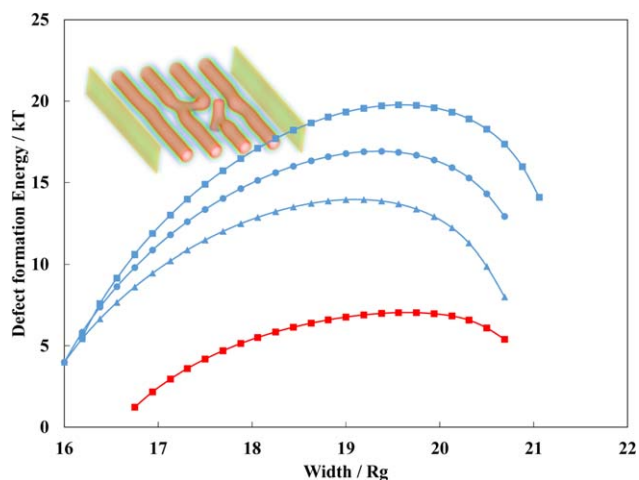


Figure 3. Plots of the dislocation (red) and the disclination (blue) formation energies for PS-b-PMMA block copolymers with various PMMA fractions. Triangles, circles, and squares correspond to fractions, $f_A = 0.23, 0.24$, and 0.25 , respectively. Only dislocations for $f_A = 0.25$ were stable. Seeded dislocations for $f_A = 0.23$ and 0.24 all melted into perfect structures. Here, $\chi N = 25$, $L_z = 3.75 R_g$, the sidewalls are A-attractive ($\chi_{wA} N = -32$), and the top and bottom are neutral. The inset shows a dislocation with a branched vertical cylinder. [Color figure can be viewed in the online issue, which is available at wileyonlinelibrary.com.]

As can be seen in Figure 3 disclination defects have higher formation energies than dislocation defects because of the extra bending energy cost necessary for the formation of disclinations. For both defects, the formation energies are nonmonotonic functions of channel width but have a maximum value at prescribed optimal widths where perfect cylinder formation is most favored. In the case of disclinations, we also observe an increase of the formation energy with increasing PMMA fractions. This effect is more pronounced on the tensile side of the commensurability window and indicates a greater bending energy cost in the presence of larger PMMA domains.

Another interesting feature of the plots in Figure 3 is the range of defect formation energies. From our simulations of the present wetting conditions, we found that formation energies are 2–7 kT for dislocations and ≈ 5 –20 kT for disclinations. These values are strikingly smaller than those computed for lamella-forming systems²⁹ in similar height and width channels where the defect formation energies are 55–90 kT for dislocations and 95–120 kT for disclinations. In addition to morphological differences between the lamellae and the cylinders, the difference lies mainly in the nature of the resulting defects in both structures. As can be seen in the inset of Figure 3, defects in cylinder-forming systems also include small vertical cylinders branching off the disconnected horizontal cylinders. The presence of these branched structures induces defect relaxation and is responsible for the low defect formation energies in Figure 3 relative to lamellar structures.

It should be noted that the emergence of branched defect structures is a consequence of the neutral wetting conditions imposed at the top and bottom surfaces. As will be described below, a modification of the wetting conditions can suppress branched cylinders and increase defect formation energies.

DSA IN A-ATTRACTIVE SIDEWALLS AND BOTTOM SUBSTRATES AND B-ATTRACTIVE TOP SURFACES

We extend in this section our investigation of various wetting conditions and explore, in particular, the effect of selective top and bottom surfaces, while maintaining the same A-attractive sidewalls from the previous section. As noted above, when the top and bottom surfaces are neutral, vertically branched cylinders form oval-shaped A-columns that lower the dislocation formation energy. In contrast, when the top and bottom surfaces are B-attractive, we have shown in a previous study³⁷ that the edges of the column become sharper with increasing affinities of the top and bottom surfaces for the B-block. For strong B-affinities, the column is completely removed and the defect formation energy is increased. In this study, we will also focus on strongly B-attractive top surfaces, but we consider only A-attractive bottom substrates. The new wetting configuration not only removes the vertical branches of the dislocation defects, but it is also most appropriate for comparisons with experimental results of Mishra et al.³² on the self-assembly of cylinder-forming PS-b-P2VP polymers in confining channels. In these experiments, P2VP (minority A) blocks wet the silicon substrate while the PS (majority B) blocks populated the polymer-air

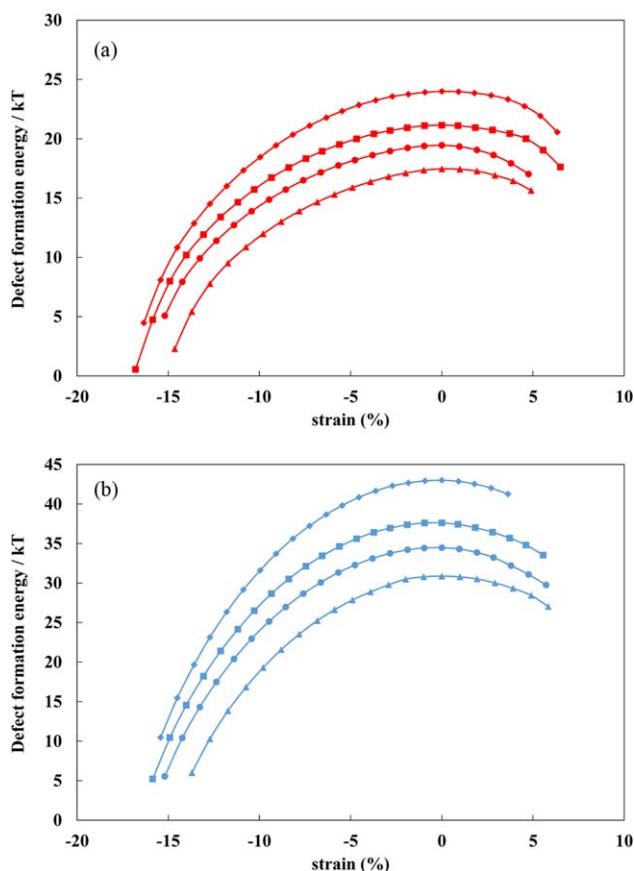


Figure 4. Plots of the dislocation (a) and the disclination (b) formation energies for confined PS-b-PMMA block copolymers with various PMMA fractions as function of the dimensionless strain. Triangles, circles, squares, and diamonds correspond to fractions, $f_A = 0.23, 0.24, 0.25,$ and 0.27 , respectively. Here, $\chi N = 30$, $L_z = 5.6 R_g$, the sidewalls and bottom substrates are A-attractive ($\chi_{wA} = -32$) and the top surface is B-attractive ($\chi_{wB} = -32$). [Color figure can be viewed in the online issue, which is available at wileyonlinelibrary.com.]

wetting layer because of the different surface energies of the two blocks.

We therefore consider polymer chains with segregation strengths $\chi N = 25, 27, 30,$ and 33 , A-fractions $f_A = 0.23, 0.24, 0.25,$ and 0.27 confined inside channels of optimized height, $L_z = 5.6 R_g$, A-attractive sidewalls and bottom substrates ($\chi_{wA} N = -32$), and B-attractive-top surfaces ($\chi_{wB} N = -32$). In our calculations, we also restrict channel widths to those leading to four periods of horizontal cylinders and introduce a dimensionless strain $(\text{width} - \text{width}_{\text{optimal}}) / (\text{width}_{\text{optimal}} \times 100)$ that measures relative deviations from the optimal width that maximizes the formation energy. By comparison, the experiments of Mishra et al.¹⁶ used PS-b-P2VP of molecular weights, 21 kg/mol ($f_{\text{PVP}} \approx 0.232$) and 26 kg/mol ($f_{\text{PVP}} \approx 0.258$), translating to $\chi N = 24.4$ and 30.2 which are very close to our model parameters.

Effect of Volume Fraction

The dislocation and disclination formation energies for confined PS-b-PMMA block copolymers with $\chi N = 30$ and various A

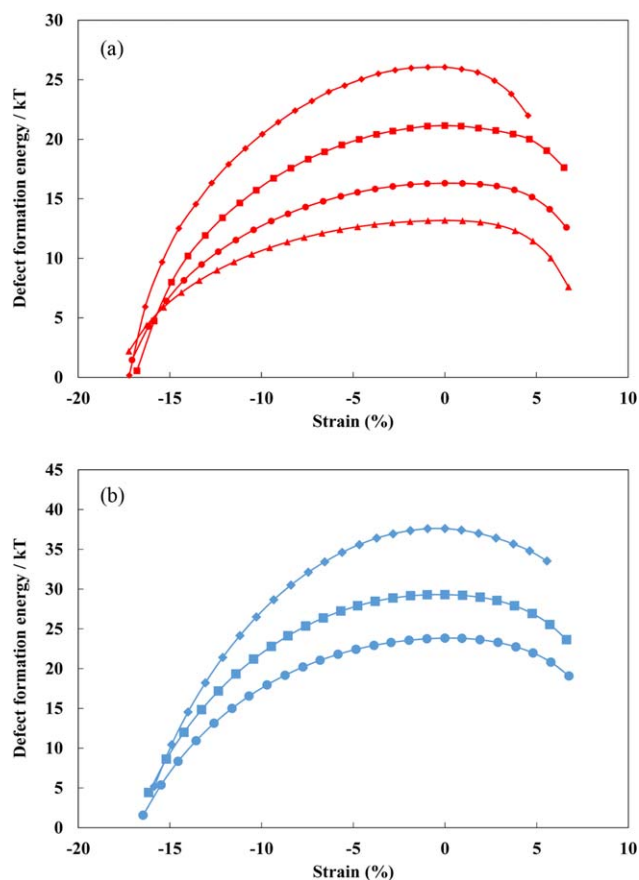


Figure 5. Plots of the dislocation (a) and disclination (b) formation energies for confined PS-b-PMMA block copolymers with various χN as function of the dimensionless strain. Triangles, circles, squares, and diamonds correspond to $\chi N = 25, 27, 30,$ and $33,$ respectively. Here, $f_A = 0.25,$ $L_z = 5.6 R_g,$ the sidewalls and bottom substrates are A-attractive ($\chi_{wA} = -32$) and the top surface is B-attractive ($\chi_{wB} = -32$). Note that disclinations in (b) were not stable for $\chi N = 25$. [Color figure can be viewed in the online issue, which is available at wileyonlinelibrary.com.]

(PMMA) block fractions are plotted in Figure 4 as function of the dimensionless strain. As can be seen in Figure 4, when changing the fraction from 0.23 to 0.27, the maximum defect formation energy increases from ≈ 17 to ≈ 24 kT for dislocations and from ≈ 31 to ≈ 43 kT for disclinations. As discussed in the introduction, the corresponding formation energies for PS-b-P2VP systems can be estimated by rescaling with a factor of 0.58. Accordingly, the predicted dislocation formation energies for PS-b-P2VP block copolymers are very close to the experimental values of ≈ 10 – 14 kT reported by Mishra et al.³² for similar systems. As the fraction of P2VP is further decreased below 0.23, the formation energy should significantly decrease (also experimentally observed), due to the low energy “disconnection” defects that result from the decay of the thinning P2VP bridge in dislocations.

Furthermore, we find from our simulations that the optimal width where the strain is zero also increases from $\approx 19 R_g$ to $\approx 21 R_g$ with increasing A-fractions. This is not a negligible shift as it represents almost half of the domain spacing.

Effect of χN

The dislocation and disclination formation energies for confined block copolymers with $f_A = 0.25$ and various χN are shown in Figure 5. The maximum dislocation defect formation energy increases from ≈ 13 kT and ≈ 26 kT as χN is increased to 30 and this result is again similar to the experimental values (10–14 kT), when the values are rescaled for PS-b-P2VP systems (7.5–15 kT). In the case of disclinations, the formation energies are about 30% larger than those observed for dislocation defects.

We also found that the position of the maximum free energy in the dislocation case only increases from $\approx 20 R_g$ to $\approx 20.7 R_g$. This is a smaller change than that observed when the composition is varied. The major difference between defect structures is the size of the minor-block bridge between the two parallel cylinders. When χN is small ($\chi N = 25$) the minor-block bridge is thinner than the bridge when χN is large ($\chi N = 33$). This is shown in the A-block density snapshot in Figure 6 with the bridge area circled in red.

OPTIMAL WETTING CONDITIONS DSA IN NARROW TRENCHES

We extend our investigations in this section to elucidate conditions in terms of the segregation strength, polymer composition and wetting conditions that are most amenable to creating defect-free monolayers of horizontal cylinders in thin, laterally confining channels. Using 3D SCFT simulations, we have computed defect formation energies for dislocations and disclinations in polymers with various χN and f_A , confined in channels of various widths (although allowing for only 4 periods) and several combinations of wetting scenarios at the sidewalls, top, and bottom surfaces of the channel. The full formation energy variations with channel widths were all found to follow the same nonmonotonic trends shown in Figures 5 and 6. For simplicity, we only report maximum values of the formation energy at the optimal width. Our results are summarized in Figure 7 for χN effects and Figure 8 for composition effects. As mentioned earlier, the reported values correspond to PS-b-PMMA block copolymers. Values for other polymers can be obtained using the scaling in eq. 2a.

Our findings suggest that using higher χN parameters enables cylindrical DSA with linearly higher defect formation energies (see Figure 7). For a fraction $f_A = 0.25$, the plots indicate that for χN values ranging from 25 to 38, the maximum defect formation energies are in the order of ≈ 10 – 39 kT for dislocations and 18–57 kT for disclinations. This increase is mainly due to the increase in the A–B interfacial energy in the distorted area generated by the defect. As χN increases, the cost of generating the area distortions also increases which results in turn in an increase in the defect formation energy. Kinetic considerations aside, large values for χN are thus preferable. One way to increase χN is to increase the total molecular weight of the polymer. This implies however that both the pitch and the domain size will also increase which can be highly undesirable if one wishes to produce reduced-size features. Moreover, high molecular weight polymers can be problematic during the annealing process, especially in the entangled regime, as they

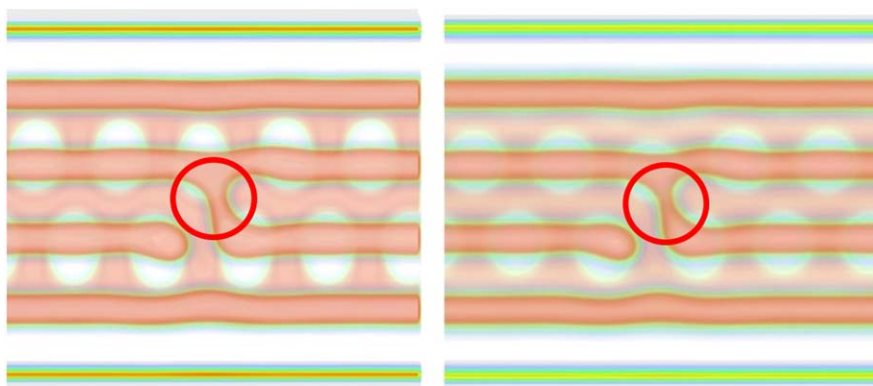


Figure 6. Examples of dislocation defects with thinning bridge between the two central cylinders. The sidewalls and bottom substrate are A-attractive ($\chi_{wA}N = -32$) and the top surface is B-attractive ($\chi_{wB}N = -32$). When χN is small ($\chi N = 25$, right), the minor-block bridge is thinner than the bridge when χN is large ($\chi N = 33$, left). [Color figure can be viewed in the online issue, which is available at wileyonlinelibrary.com.]

can induce kinetically trapped defects that will require very long times to heal. Choosing a diblock copolymer with a higher χ value, such as PS-b-P2VP or PS-b-PDMS for example, can alleviate this problem and enables larger χN while maintaining relatively low molecular weights.

Similar to the effect of segregation strength, higher fractions of the A-block result in higher defect formation energies. For $\chi N = 30$, Figure 8 shows that an increase of f_A from 0.23 to 0.3 yields an increase of the maximum formation energy by ≈ 5 – 10 kT for dislocations and by ≈ 10 to ≈ 15 kT for disclinations. While this is highly desirable, the minor block composition cannot exceed $f_A = 0.33$, which is the upper boundary before lamellar structures are formed.³⁸

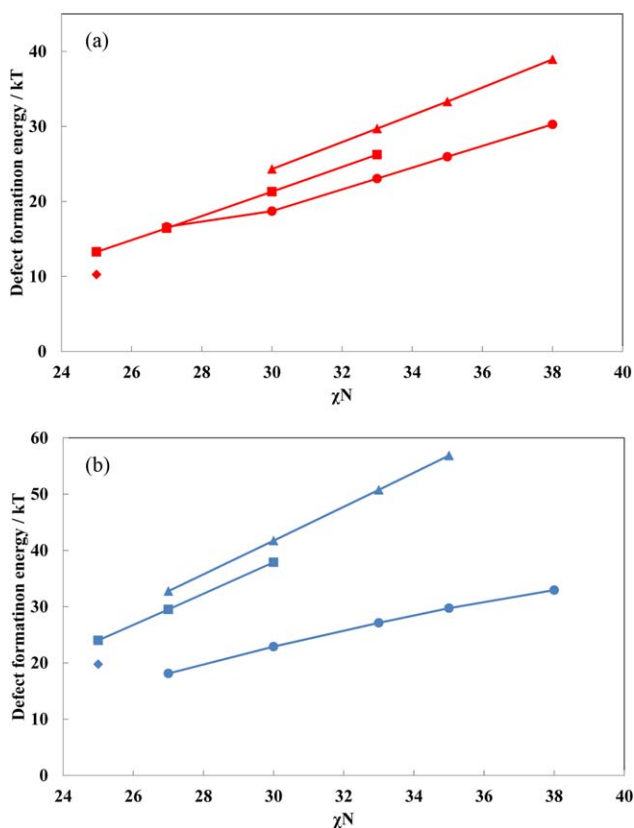


Figure 7. Plots of the dislocation (a) and the disclination (b) formation energies for confined PS-b-PMMA block copolymers as a function χN inside channels with various wetting conditions at the sidewalls(s), bottom substrate (b) and top (t) surfaces. Triangles, squares, circles, and diamonds correspond to $[A(t), B(s+b)]$, $[A(s+b), B(t)]$, $[A(s+b+t)]$, and $[A(s)]$ wetting configurations, respectively. [Color figure can be viewed in the online issue, which is available at wileyonlinelibrary.com.]

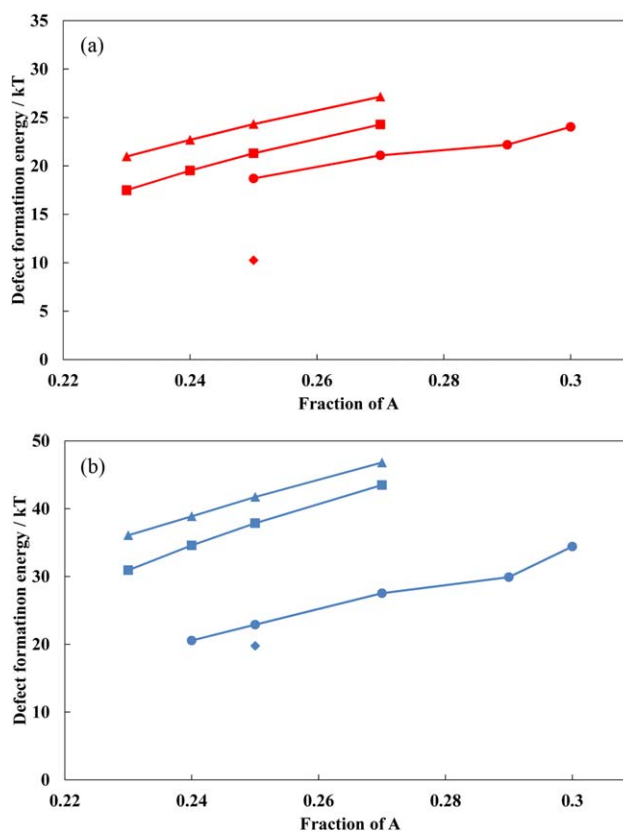


Figure 8. Same as Figure 7 for the effect of varying f_A . [Color figure can be viewed in the online issue, which is available at wileyonlinelibrary.com.]

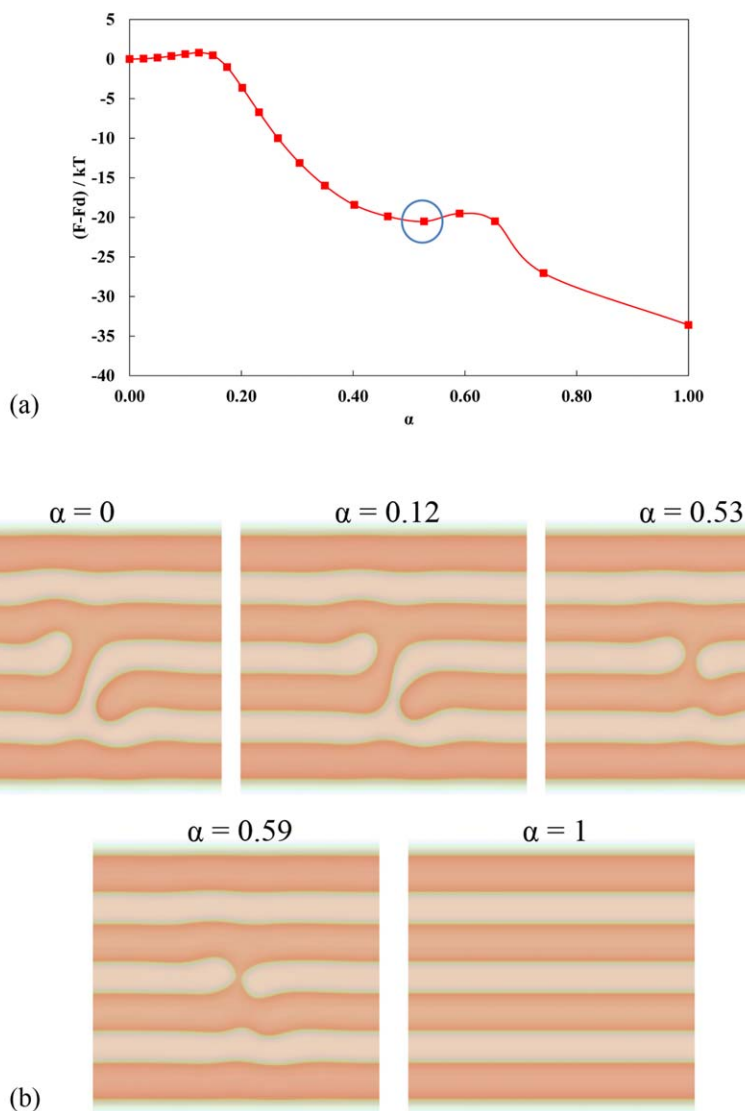


Figure 9. (a) Example of a kinetic pathway for the melting of a dislocation defect when $\chi N = 33$, width = $18 Rg$, $\chi_w N = -64$. (b) Density profiles of the 5 extrema states in (a). The metastable state at $\alpha = 0.53$ corresponds to the single-bridge-double-contact (SBDC) defect (blue circle). [Color figure can be viewed in the online issue, which is available at wileyonlinelibrary.com.]

Turning on either B- or A-selectivities at the top and bottom surfaces whilst maintaining A-attractive wetting conditions only on the sidewalls [the $A(s)$ wetting configuration in Figures 7, 8] enables an additional formation energy gain of $\approx 5\text{--}10$ kT for both dislocation and disclination defects. This is mainly the result of the wetting conditions that remove the formation of vertically branched cylinders at the end of the defect area as shown in section “Defectivity”. As can be seen in both Figures 7 and 8, B-attractive sidewalls and bottom substrates and A-attractive top surfaces ($A(t) + B(s + b)$) yield the highest defect formation energies for both dislocations and disclinations. If the selectivities are switched to ($A(s + b) + B(t)$), the formation energies are lowered by ≈ 5 kT. An additional decrease of ≈ 5 kT is also observed with all A-attractive surfaces ($A(s + b + t)$). Finally, as mentioned above, setting the top and bottom surfaces to neutral, yields the lowest formation energies and is therefore most conducive for stable defects in the narrow trenches.

While the results shown above can provide useful guidelines for the design of optimized and low defect-density graphoepitaxial processes, annealing conditions and kinetics of defect melting into perfect structures are equally important. The transition pathways and the kinetic barriers are discussed in the next section.

DEFECT KINETICS: TRANSITION PATHWAYS AND KINETIC BARRIERS

Outline of the String Method

The string method^{30,31} is a numerical technique capable of finding local minimum energy paths (MEPs) between two locally stable wells (in our case a metastable defect state and a stable perfect state) in a high-dimensional free energy landscape. This technique entails creating a discrete sequence, or string, of field configurations with endpoints lying within the basin of attraction of the two metastable states. The intermediate

configurations are initialized in such a way that they gradually cross the barrier, or barriers, from one basin of attraction to the other. This can be accomplished, for example, via a linear interpolation between the two endpoints, although this is by no means the only way to initialize the string. The string is then evolved according to the following two-step algorithm. First, each image is relaxed individually for one time step in the direction of a local force calculated from gradients in the mean field (SCFT) free energy landscape. Following the update step, each configuration will have relaxed towards the nearest basin of attraction. To offset this effect and avoid skewed distributions of field configurations along the string, a second reparameterization step is performed using a smooth interpolation between neighboring configurations. This two-step process is repeated until the intermediate configurations lie along a local MEP connecting one basin to the other, with each endpoint at the bottom of its respective stable or metastable well. The string method is guaranteed to converge to a local MEP, but the global free energy landscape may contain several local MEPs (e.g., a symmetric path and asymmetric path for disclination melting), in which case the local MEP to which the string eventually converges depends on how the interior configurations are initialized. For this reason, in addition to the simple method of linear interpolation between endpoints, our implementation also allows us to load custom interior configurations to seed multiple expected pathways.

The detailed implementation of the string method and its particular application to field theories for block copolymers can be found elsewhere.^{30,31,39}

Melting Mechanisms

The string method outlined above was implemented using NVIDIA's CUDA framework to develop fast and efficient GPU-based 3D calculations of transition pathways in DSA environments and, in particular, for our current DSA application of cylinder-forming block copolymers in narrow trenches. Following the extensive study of optimal wetting scenarios in section "Optimal Wetting Conditions DSA in Narrow Trenches", we only consider for string calculations trenches with B-attractive sidewalls and bottom substrates ($\chi_{wB}N = -32$) and A-attractive top surfaces ($\chi_{wA}N = -32$). While this wetting configuration is more easily established for PS-*b*-PDMS systems,^{13,36} the energy barriers and transition rates presented in this section are calculated for PS-*b*-PMMA for consistency with the thermodynamic calculations above. A scaling factor of 0.35 should be introduced for energy barriers in PS-*b*-PDMS systems.

For a PS-*b*-PMMA block copolymer with $\chi N = 33$, and $f_A = 0.3$, we plot in Figures 9–11 examples of MEP calculations for the transition of dislocations and disclinations to perfect states in channels with width $Lx = 18 R_g$ and height $= 6 R_g$. All our string calculations, exemplified in Figure 9(a), led to MEPs with multiple transition barriers for dislocations, contrasting with previous calculations on lamella-forming block copolymers where all dislocations resulted in melting mechanisms with a single barrier.²⁹ A closer look at the density profiles of Figure 9(b) reveal that, starting at a dislocation ($\alpha = 0$), the chains in the defect core region must rearrange to

connect the two ends of the broken cylinder forming the dislocations. The excess interfacial area during this step results in the first kinetic barrier (first local maximum along the MEP), at a transition state $\alpha = 0.12$. Once the two ends have fully merged, the melting of the defect proceeds until a second metastable state is reached at $\alpha = 0.53$. As shown in Figure 9(b), the intermediate metastable defect consists of a narrow single A block bridge between the two continuous cylinders. For discussions below, this single-bridge-double-contact defect will be referred to as a SBDC defect. When the system has crossed the second barrier at the transition state $\alpha = 0.59$, the bridge connecting the two A-cylinders breaks and a defect-free configuration is formed at $\alpha = 1$. As seen in Figure 9(a), the two kinetic barriers for the melting of a dislocation are very small (less than 1–2 kT), mainly resulting from the minimal mixing of the A- and B-blocks during the melting process.

In the case of disclinations, the examples in Figures 10 and 11 show that the melting pathways of disclinations are not unique, a feature that was also observed in a previous application of the string method to lamella-forming block copolymers.²⁹ When the string is initialized with a simple linear interpolation between the disclination and the perfect structure, a symmetric 2-barrier melting pathway takes place in Figure 10(a). In this process, after crossing a first transition state at $\alpha = 0.13$, the two PMMA bends of the double-disclination defect simultaneously and symmetrically meet to form a new metastable defect at $\alpha = 0.55$. In contrast to the melting of dislocations, the inner metastable defect has two narrow bridges between the two adjacent cylinders, with a roughly circular hole dividing them. It will consequently be referred to as a double-bridge-double-contact, or DBDC defect. A subsequent thinning of the two bridges culminates at a second kinetic barrier at a transition state $\alpha = 0.62$, after which perfect cylinders are produced. The symmetry of this mechanism can be broken (through thermal fluctuations for example) in favor of asymmetric pathways. For example, when the initial string is seeded with a dislocation at some interior field configuration, an asymmetric 4-barrier melting pathway develops during the transition from a disclination to the perfect state. In this process, Figure 11(a) of the converged 4-barrier MEP string shows that a first kinetic barrier is found at the transition state $\alpha = 0.08$ whereby a single connection develops between the two bends and produces a second metastable defect at $\alpha = 0.26$, referred to henceforth as a double-bridge-single-contact, or DBSC defect. The two disconnected parts of the center cylinder are now fully merged and the other two parts from the adjacent cylinder and joined to the center cylinder by narrow bridges, remain to be connected. As the melting proceeds, one of the two bridges connecting the broken ends to the center cylinder weakens until it disappears and gives way to a new metastable state at $\alpha = 0.53$, found to be a dislocation. From this point on, the pathway proceeds to a perfect morphology following the 2-barrier mechanism described above for the melting of dislocations. While the barriers for both the symmetric and asymmetric pathways are relatively small (< 2 kT), the strings in Figures 10 and 11, suggest that the low barrier leading to a

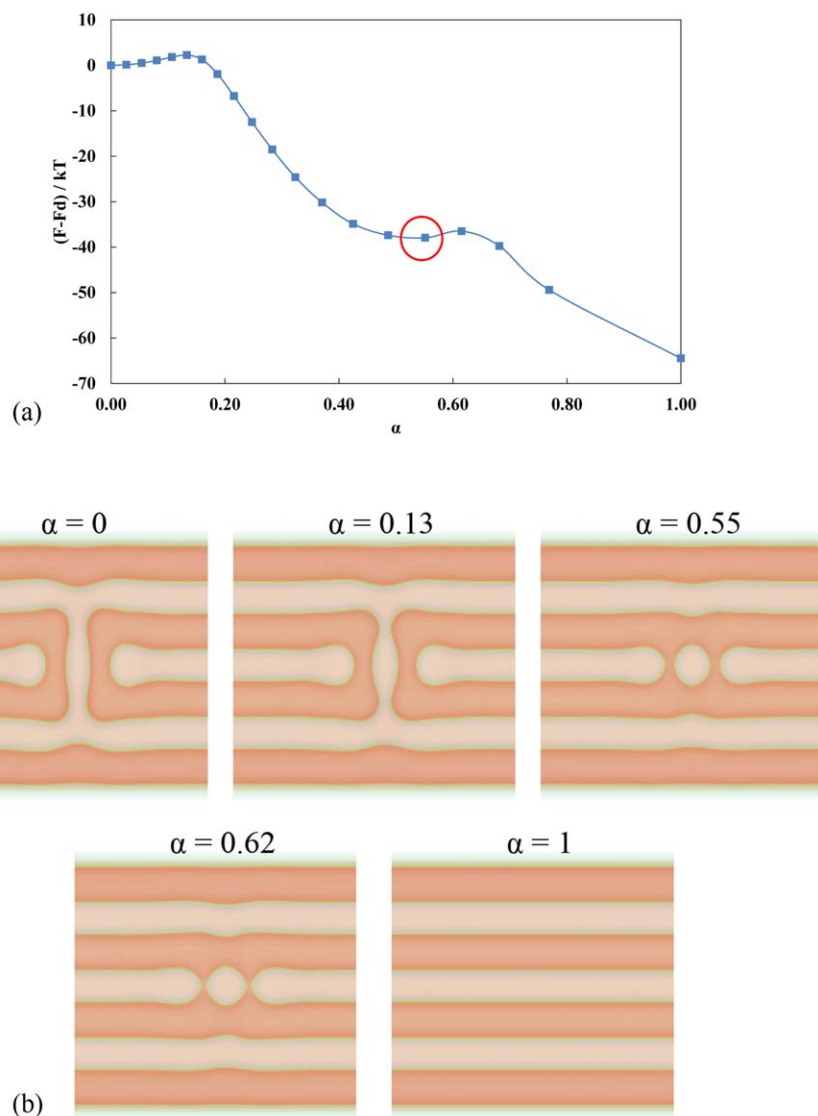


Figure 10. (a) Example of a symmetric kinetic pathway for the melting of a disclination defect when $\chi N = 33$, width = $18 R_g$, $\chi_w N = -64$. (b) Density profiles of the five extrema states in (a). The metastable state at $\alpha = 0.55$ corresponds to the double-bridge-double-contact (DBDC) defect (red circle). [Color figure can be viewed in the online issue, which is available at wileyonlinelibrary.com.]

dislocation in the asymmetric pathway will result in faster melting rates compared to symmetric pathways.

Commensurability Effects

Beyond elucidating the melting mechanisms and the details about the minimum energy paths, such as the presence of intermediate metastable states and additional barriers to the final state, we have also explored the effect of commensurability on kinetic barriers during the melting of both disclinations and dislocations.

As shown in Figure 12(a), the symmetric pathway for the melting of disclinations entails large and substantially different kinetic barriers. While both barriers are nonmonotonic, they have minimum values at different channel widths. The first barrier, corresponding to the transition of the disclination to the DBDC defect, has a minimum at a width $\approx 18.1 R_g$, close to the channel commensurability width of $\approx 17.9 R_g$. However, the

minimum value of the second barrier occurs at a slightly narrower channel width of $\approx 16.8 R_g$. Note also that for most channel dimensions ($\leq 18.6 R_g$), a symmetric pathway will produce DBDC defects from disclinations at a slower rate than the complete melting of the former into perfect structures; the second barrier ($\approx 1-2$ kT) is lower than the first barrier ($\approx 2.2-4.2$ kT) for channel widths $< 18.6 R_g$. As the channel width is increased beyond $18.6 R_g$, more DBDC defects will be long lived in the melt as their production rate (first barrier $\approx 2.5-3$ kT) will exceed their removal rate (second barrier $\approx 2.5-7$ kT).

The presence of DBDC defects is also contingent on the production of DBSC and dislocation defects during the asymmetric melting of disclinations. The kinetic barriers for the four transition states of the asymmetric pathway are plotted in Figure 12(b), as a function of channel widths (note that the third and fourth barriers correspond to the first and second barriers for the melting of dislocations). Similar to the symmetric case, the

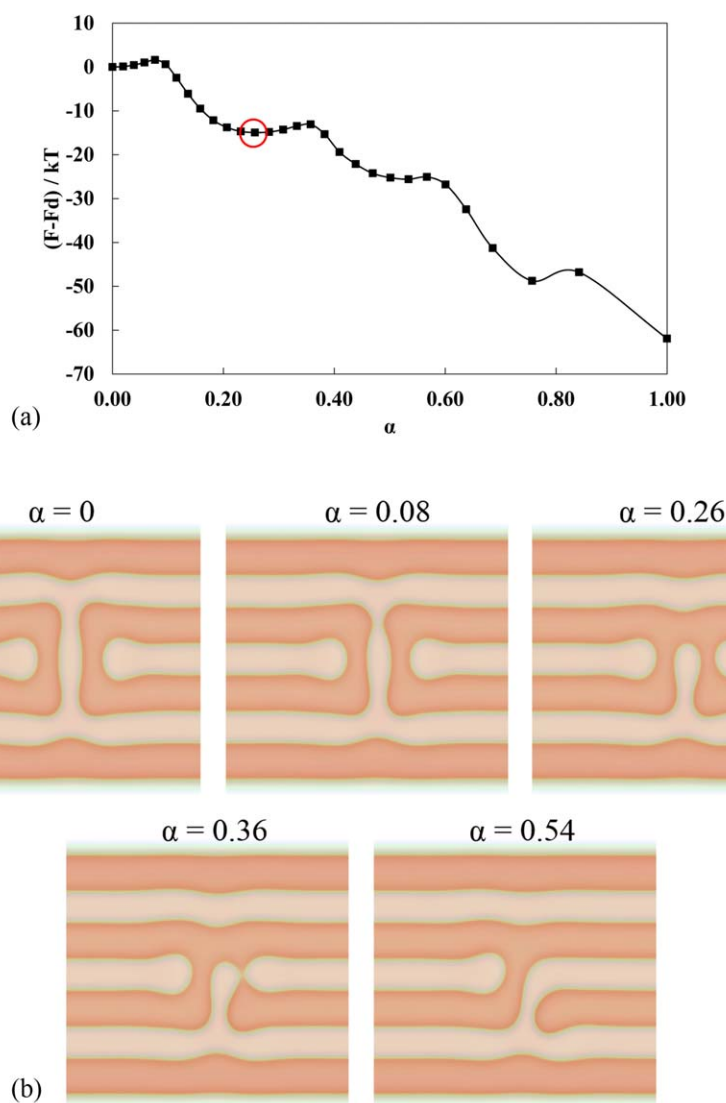


Figure 11. (a) Example of an asymmetric kinetic pathway for the melting of a disclination defect when $\chi N = 33$, width = $18 R_g$, $\chi_{in} N = -64$. (b) Density profiles of the first five extrema states in (a), showing the melting of the disclinations into a dislocation. The extrema states from the dislocation to the perfect state are similar to those shown in Figure 9(b). The metastable state at $\alpha = 0.26$ corresponds to the double-bridge-single-contact (DBSC) defect (red circle). [Color figure can be viewed in the online issue, which is available at wileyonlinelibrary.com.]

first and second barriers, leading to dislocations, can vary quite broadly over changes in channel dimensions. Likewise, the relative magnitudes of the two barriers also depend on channel width, thereby affecting the rate of production and removal of the DBSC and dislocation defects. In addition, the third and fourth barriers are quite small, with values ≈ 0.25 kT in the vicinity of the commensurability width. Away from optimal conditions, these barriers increase sharply to ≈ 2 kT, resulting in a ≈ 6 -fold increase in the time required for the annihilation of dislocations. The plots of the third and fourth barriers also suggest that the production of SBDC defects will always be faster than their decay into defect-free morphologies (the third barrier is always lower than the fourth barrier). Overall, the barriers for the melting of dislocations and SBDC defects are quite small as compared to barriers for the melting of DBDC, DBSC, and disclination defects. In other words, if a certain distribution of defects is initially present in the melt, dislocations will be the

fastest to heal to perfect structures, even when disclinations follow a symmetric pathway that avoids the formation of intermediate dislocations. In what follows, we present a quantitative description of the melting rates and the time-evolution of a population of isolated, independent defects in the melt.

Melting Mechanisms: Examples of Reaction-Rate Calculations

By solving simple reaction-rate equations connecting stable or metastable states identified from the converged MEPs, we can estimate the concentrations of the various defective morphologies present in the melt at any given time. The melting of dislocations can be represented by the following reaction:



where (DISL) and (P) are the dislocation and the perfect states, respectively, and the intermediate SBDC defect is shown in

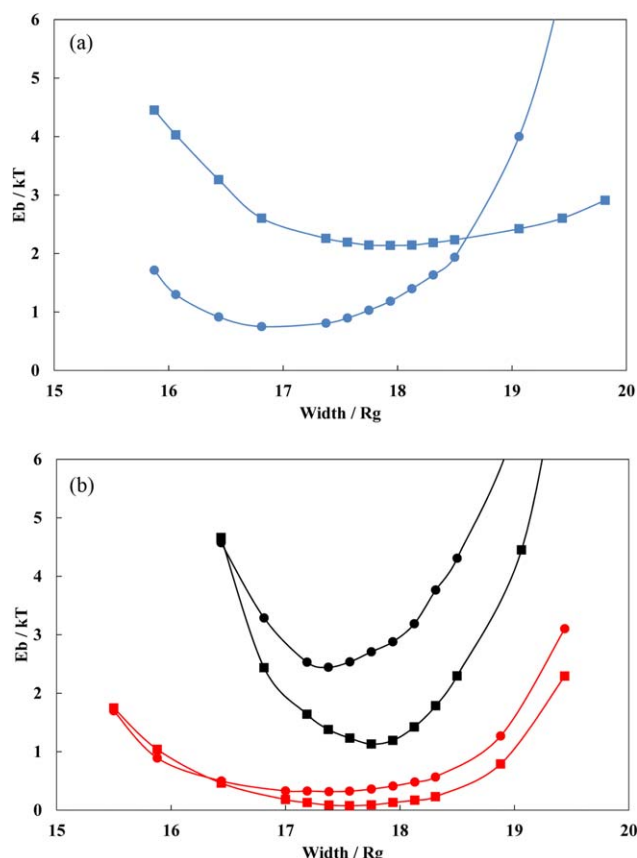
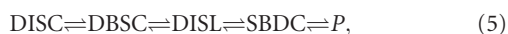


Figure 12. (a) Plots of the first (square) and second (circle) barrier heights, E_b , as a function of the channel width for the symmetric melting of disclination defects. (b) Plots of the first (square, black), second (circle, black), third (square, red), and fourth (circle, red) barrier heights, E_b , as a function of the channel width for the asymmetric melting of disclination defects. Note that the third and fourth barriers correspond to the first and second barriers for the melting of a dislocation defect. [Color figure can be viewed in the online issue, which is available at wileyonlinelibrary.com.]

Figure 9(b). Likewise, the symmetric and asymmetric pathways for disclinations, respectively, can be written as:



where (DISC) is the disclination defect and the other defects are shown in Figures 10(b) and 11(b). Using a Kramers-like approach, the kinetic rate, $k_{1 \rightarrow 2}$, of the transition from state (1) to state (2) is

$$k_{1 \rightarrow 2} = \tau_0^{-1} e^{-E_b/kT} \quad (6)$$

where E_b is the barrier height for the transition from (1) to (2) and τ_0 is the time necessary for diffusion of chains parallel to the microdomain interfaces over a distance comparable to the size of the defect.²⁹ In the case of PS-PMMA at a molecular weight corresponding to $\chi N = 25$ for example, $\tau_0 \approx 9$ s.²⁹

To better illustrate the tradeoffs outlined above with regard to commensurability, we consider three different channel widths = 18, 19.4, and 16.4 R_g , corresponding to widths very close to, wider than, and smaller than the perfect state

Table I. Barrier Heights of the Various Transitions in Eqs. 3–5 for Three Different Channel Widths = 18, 19.4, and 16.4 R_g

Reaction	Kinetic barriers (in units of kT)		
	18 R_g	19.4 R_g	16.4 R_g
DISL \rightarrow SBDC	0.13	2.29	0.46
SBDC \rightarrow DISL	21.54	20.96	17.93
SBDC \rightarrow P	0.42	3.10	0.50
P \rightarrow SBDC	14.16	10.79	13.21
DISC \rightarrow DBDC	2.13	2.60	3.26
DBDC \rightarrow DISC	27.01	21.98	25.19
DBDC \rightarrow P	1.18	6.60	0.91
P \rightarrow DBDC	34.70	28.30	27.26
DISC \rightarrow DBSC	1.19	4.45	4.66
DBSC \rightarrow DISC	16.00	17.03	12.66
DBSC \rightarrow DISL	2.88	6.97	4.57
DISL \rightarrow DBSC	13.11	10.05	8.08

commensurability width, respectively. The barrier heights of the various transitions in eqs. 3–5 are summarized in Table I.

Assuming Boltzmann statistics for the initial defect distributions, one can set the initial defect concentrations based on their formation energies. From our converged MEP strings, we found that the formation energies of SBDC defects are several tens of kT smaller than those of all other defects, resulting in a unimodal initial defect distribution that very quickly relaxes to a defect-free structure given the low kinetic barrier for the melting of SBDC defects [<1 – 2 kT from Figure 12(b)]. Nevertheless, since other defects can also be kinetically trapped initially in the melt and to keep our approach simple and informative, we consider a situation where only disclinations are present in the melt at time, $t = 0$ and monitor the evolution of the various defect

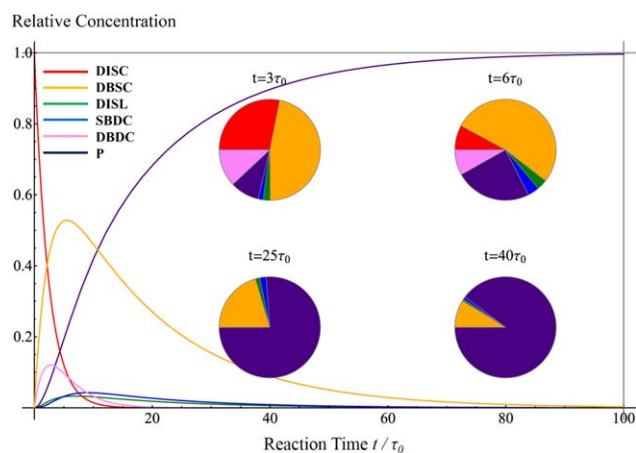


Figure 13. Time evolution of the relative concentrations of the five metastable defects and the perfect state inside channels with width = 18 R_g . The four pie chart insets represent the relative concentrations of the six states at times, $t = 3 \tau_0$, $6 \tau_0$, $25 \tau_0$, and $40 \tau_0$. [Color figure can be viewed in the online issue, which is available at wileyonlinelibrary.com.]

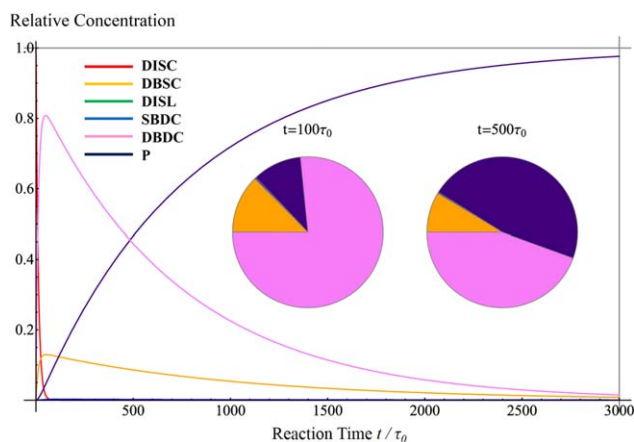


Figure 14. Same as Figure 13 for a channel width = $19.4 R_g$. [Color figure can be viewed in the online issue, which is available at wileyonlinelibrary.com.]

concentrations at later times t , plotted in Figures 13–15 for the three channel widths introduced above.

In channels close to optimal widths, Figure 13 shows the annealing time required for a 99% melting of all defects is $\approx 100 \tau_0$, several times smaller than for defect annihilation in channels away from commensurability. The plots in Figures 14 and 15 show the same annealing times are $3000 \tau_0$ and $500 \tau_0$ at channel widths $19.4 R_g$ and $16.4 R_g$, respectively, emphasizing not only the thermodynamic but also the kinetic role of optimal design for the confining trenches.

More specifically, the plots in Figure 13 indicate that the initial disclinations under optimal conditions first transform into DBSC and DBDC defects; at time $t = 3 \tau_0$ [DBSC] $\approx 47\%$ and [DBDC] = 12%. As the disclinations start to melt, the formed DBDC defects from the symmetric pathway are removed at fast rates in favor of perfect structures while the concentrations of DBSC defects continue to grow. This situation is shown in the pie chart in Figure 13 at times $t < 10 \tau_0$. As time proceeds, the remaining DBDC defects continue their melting at slow rates. The ensuing dislocations almost immediately change into DBSC

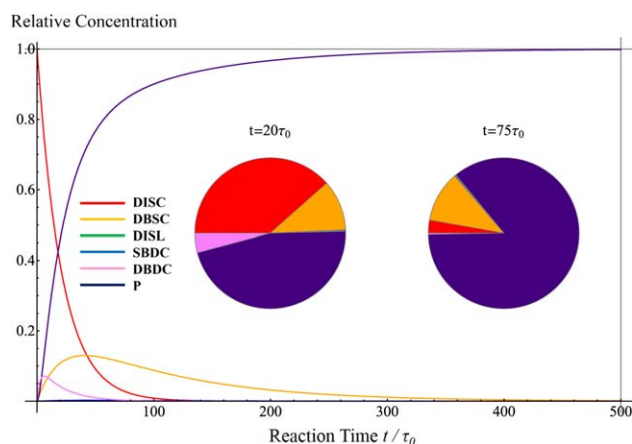


Figure 15. Same as Figure 13 for a channel width = $16.4 R_g$. [Color figure can be viewed in the online issue, which is available at wileyonlinelibrary.com.]

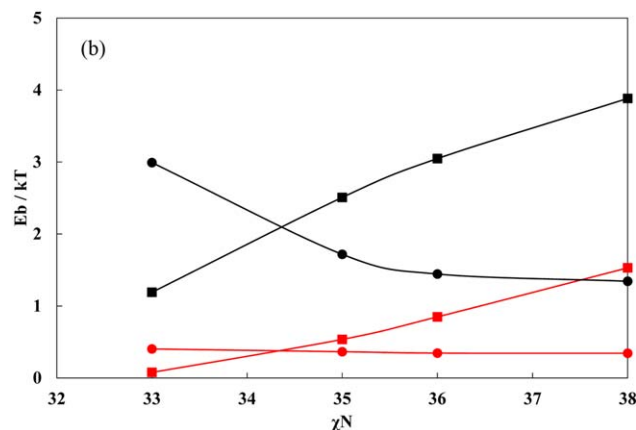
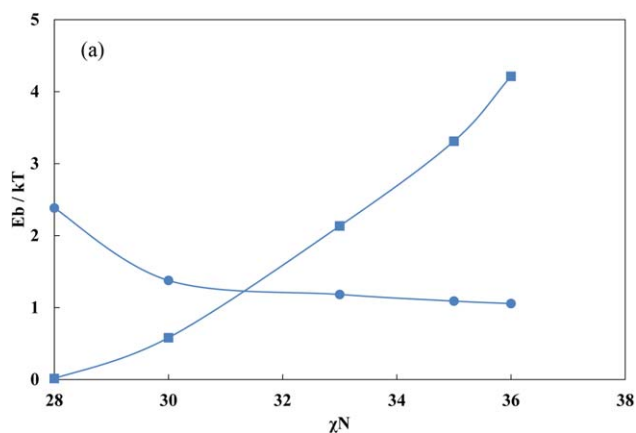


Figure 16. (a) Plots of the first (square) and second (circle) barrier heights, E_b , as a function of χN for the symmetric melting of disclination defects in channels with width = $18 R_g$. (b) Plots of the first (square, black), second (circle, black), third (square, red), and fourth (circle, red) barrier heights, E_b , as a function of χN for the asymmetric melting of disclination defects in channels with width = $18 R_g$. Note that the third and fourth barriers correspond to the first and second barriers for the melting of a dislocation defect. [Color figure can be viewed in the online issue, which is available at wileyonlinelibrary.com.]

defects, which themselves change into perfect structures at a similar rate; thereby, maintaining both dislocations and SBDC defects at low concentrations ($< 5\%$). The pie chart at times $t > 20 \tau_0$ exemplifies the fast production and removal of dislocation and SBDC defects.

At a channel width = $19.4 R_g$, Figure 14 indicates the initial disclinations quickly and almost completely merge to form DBDC defects following a symmetric melting pathway. After $t = 100 \tau_0$, the distribution of defects is dominated by DBDC defects as shown in the pie chart of Figure 14. At later times, the DBDC defects slowly decay into perfect structures due to the relatively high kinetic barrier governing this process (≈ 6.60 kT from Table I). Beyond $t = 500 \tau_0$, the melt also contains some DBSC defects, albeit at lower concentrations ($< 10\%$). Other defects also remain at very low concentrations during the melting, never exceeding 1%.

The melting pathways are the simplest when the channel width is at $16.4 R_g$. As seen in Figure 15, the initial set of disclinations is slowly removed from the system with the appearance of

transient DBDC and DBSC defects during the process. Other defects are generated and removed from the melt at nearly similar rates and hence their concentrations are kept at very low levels, below 1–2%.

Effect of χN

We now consider the effect of the segregation strength on transition barriers. The two barriers for the symmetric melting of disclinations are plotted in Figure 16(a) at a height = $6 R_g$ and a width = $18 R_g$, very close to the commensurability widths at each χN of interest. Likewise, the four barriers for the asymmetric pathways are plotted in Figure 16(b) at similar channel dimensions. (Note again that the third and fourth barriers of the asymmetric pathway are the same as the first and second barriers for the melting of dislocations.)

While the kinetic barriers for the melting of dislocations remain rather low (<1 kT) when χN is increased, the first and second barriers for the symmetric and asymmetric melting of disclinations can range from 1 to 4 kT. The first barrier always increases with χN as it is associated with an excess interfacial area and stretching of the chains necessary to connect the two broken parts of the center cylinders leading to DBDC and DBSC defects. In contrast, the second barriers are associated with a thinning of the bridges between the cylinders. Since this process apparently does not require an excess interfacial area or additional stretching of the chains, the second barrier is a decreasing function of χN . The two opposite trends of the first and second barriers indicate that the segregation strength will greatly influence the production and removal rate of various metastable defects in the melt, thereby affecting their overall concentrations during the annealing process.

CONCLUSIONS

The application of block copolymer lithography to semiconductor IC patterning requires the strong suppression of native defects that form during the self-assembly process. Optimization of directed self-assembly strategies and identification of conditions that deter defect formation are required in order to achieve defect densities consistent with ITRS targets of 0.01 defects/cm². Using polymer SCFT-based simulation methods, we have demonstrated an approach for investigating equilibrium defect densities, as well as for determining kinetic pathways, free-energy barriers and an estimation of kinetic rates for removing trapped metastable defects through annealing. We have shown that, at equilibrium, the density of isolated dislocation-type and disclination-type defects in cylinder-forming diblock copolymers confined to a narrow trench with strongly selective wall wetting conditions can be well below target densities. After optimizing the wetting conditions, we find that the least defective structures follow from major-block wetting at the side walls and substrate, together with minor-block wetting on the top (polymer–air) surface.

The free energies of defect formation for both dislocations and disclinations in cylinder-forming block copolymers are approximately 30–50% of those found in lamellar-forming compositionally symmetric diblock copolymers. We find that the free energy of defect formation can be made to exceed a critical

value required to achieve equilibrium defect concentrations below the ITRS target. The remaining concern is then the ability to rapidly “melt” trapped metastable defects that can occur at much greater than equilibrium concentrations during quench. Melting of elementary defects into a perfectly ordered state requires overcoming one or more kinetic barriers, which we have calculated under various interaction conditions using the combination of SCFT and string methods. Working at optimal (commensurate) trench widths, the free-energy barrier for removal of defects is approximately 10% of that found for lamellar-forming symmetric block copolymers. We therefore predict that trapped dislocation and disclination defects can be annealed out (down to equilibrium concentrations) within tens of seconds for cylinders, whereas the same process would require several minutes to many hours for lamellae. In this regard, we predict that cylinder-forming block copolymer formulations will be superior to lamella-forming counterparts for attaining low-defectivity DSA patterning. Our findings should provide useful guidelines for the design of optimized patterning processes with low defect concentrations.

ACKNOWLEDGMENTS

We acknowledge helpful discussions with Drs. P. Trefonas, P. Hustad, J. Weinhold, V. Ginzburg, and M. Christianson from The Dow Chemical Company. We thank The Dow Chemical Company and The Dow Materials Institute at the University of California, Santa Barbara for financial support. The computer simulations presented in this work were performed using computational facilities at the California NanoSystems Institute (CNSI) and Materials Research Laboratory (MRL) at the University of California–Santa Barbara. The MRL Central Facilities are supported by the MRSEC Program of the NSF under Award No. DMR 1121053; a member of the NSF-funded Materials Research Facilities Network (<http://www.mrfn.org>).

REFERENCES

1. Caille, A. *C.R. Hebd. Sean. Acad. Sci.* **1972**, *274*, 891.
2. Herr, D. J. C. *J. Mater. Res.* **2011**, *26*, 122.
3. Park, C.; Yoon, J.; Thomas, E. L. *Polymer* **2003**, *44*, 7779.
4. Segalman, R. A. *Mater. Sci. Eng. R* **2005**, *48*, 191.
5. Angelescu, D. E.; Waller, J. H.; Adamson, D. H.; Register, R. A.; Chaikin, P. M. *Adv. Mater.* **2007**, *19*, 2687.
6. Kramer, E. J. *Nature* **2005**, *437*, 824.
7. Segalman, R. A.; Hexemer, A.; Hayward, R. C.; Kramer, E. J. *Macromolecules* **2003**, *36*, 3272.
8. Segalman, R. A.; Schaefer, K. E.; Fredrickson, G. H.; Kramer, E. J.; Magonov, S. *Macromolecules* **2003**, *36*, 4498.
9. Cheng, J. Y.; Ross, C. A.; Smith, H. I.; Thomas, E. L. *Adv. Mater.* **2006**, *18*, 2505.
10. Ito, T.; Okazaki, S. *Nature* **2000**, *406*, 1027.
11. Park, S.; Stoykovich, M. P.; Ruiz, R.; Zhang, Y.; Black, C. T.; Nealey, P. F. *Adv. Mater.* **2007**, *19*, 607.
12. Segalman, R. A.; Yokoyama, H.; Kramer, E. J. *Adv. Mater.* **2001**, *13*, 1152.

13. Cheng, J. Y.; Ross, C. A.; Chan, V. Z. H.; Thomas, E. L.; Lammertink, R. G. H.; Vancso, G. J. *Adv. Mater.* **2001**, *13*, 1174.
14. International Technology Roadmap for Semiconductors. <http://www.itrs.net>. Accessed on 1 December 2013.
15. Morkved, T. L.; Lu, M.; Urbas, A. M.; Ehrichs, E. E.; Jaeger, H. M.; Mansky, P.; Russell, T. P. *Science* **1996**, *273*, 931.
16. Pelletier, V.; Adamson, D. H.; Register, R. A.; Chaikin, P. M. *Appl. Phys. Lett.* **2007**, *90*, 163105.
17. Angelescu, D. E.; Waller, J. H.; Adamson, D. H.; Deshpande, P.; Chou, S. Y.; Register, R. A.; Chaikin, P. M. *Adv. Mater.* **2004**, *16*, 1736.
18. Kim, S. O.; Solak, H. H.; Stoykovich, M. P.; Ferrier, N. J.; de Pablo, J. J.; Nealey, P. F. *Nature* **2003**, *424*, 411.
19. Liu, C. C.; Ramirez-Hernandez, A.; Han, E.; Craig, G. S. W.; Tada, Y.; Yoshida, H.; Kang, H. M.; Ji, S. X.; Gopalan, P.; de Pablo, J. J.; Nealey, P. F. *Macromolecules* **2013**, *46*, 1415.
20. Bitá, I.; Yang, J. K. W.; Jung, Y. S.; Ross, C. A.; Thomas, E. L.; Berggren, K. K. *Science* **2008**, *321*, 939.
21. Park, S.; Lee, D. H.; Xu, J.; Kim, B.; Hong, S. W.; Jeong, U.; Xu, T.; Russell, T. P. *Science* **2009**, *323*, 1030.
22. Sundrani, D.; Sibener, S. J. *Macromolecules* **2002**, *35*, 8531.
23. Bosse, A. W.; Garcia-Cervera, C. J.; Fredrickson, G. H. *Macromolecules* **2007**, *40*, 9570.
24. Ginzburg, V. V.; Weinhold, J. D.; Trefonas, P. J. *Polym. Sci. Part B: Polym. Phys.* **2013**, doi: 10.1002/polb.23365.
25. Ruiz, R.; Sandstrom, R. L.; Black, C. T. *Adv. Mater.* **2007**, *19*, 587.
26. Toner, J.; Nelson, D. *Phys. Rev. B* **1981**, *23*, 316.
27. Hammond, M. R.; Cochran, E.; Fredrickson, G. H.; Kramer, E. J. *Macromolecules* **2005**, *38*, 6575.
28. Nagpal, U.; Muller, M.; Nealey, P. F.; de Pablo, J. J. *ACS Macro. Lett.* **2012**, *1*, 418.
29. Takahashi, H.; Laachi, N.; Delaney, K. T.; Hur, S.-M.; Weinheimer, C. J.; Shykind, D.; Fredrickson, G. H. *Macromolecules* **2012**, *45*, 6253.
30. E, W. N.; Ren, W. Q.; Vanden-Eijnden, E. *J. Chem. Phys.* **2007**, *126*, 164103.
31. Weinan, E.; Ren, W. Q.; Vanden-Eijnden, E. *Phys. Rev. B* **2002**, *66*, 052301.
32. Mishra, V.; Fredrickson, G. H.; Kramer, E. J. *ACS Nano* **2012**, *6*, 2629.
33. Stewart, M. D.; Johnson, S. C.; Sreenivasan, S. V.; Resnick, D. J.; Willson, C. G. *J. Microlith. Microfab.* **2005**, *4*.
34. Fredrickson, G. H. *The Equilibrium Theory of Inhomogeneous Polymers*; Clarendon Press: Oxford, **2006**.
35. Hur, S.-M.; Garcia-Cervera, C. J.; Kramer, E. J.; Fredrickson, G. H. *Macromolecules* **2009**, *42*, 5861.
36. Cheng, J.; Mayes, A. M.; Ross, C. A. *Nat. Mater.* **2004**, *3*, 823.
37. Kim, B.; Laachi, N.; Fredrickson, G. H. *Proc. SPIE* **2013**, *8680*, 868016.
38. Matsen, M. W.; Bates, F. S. *Macromolecules* **1996**, *29*, 1091.
39. Cheng, X. Y.; Lin, L.; E, W. N.; Zhang, P. W.; Shi, A. C. *Phys. Rev. Lett.* **2010**, *104*, 148301.